

² **Commissioning of the highly granular SiW-ECAL 3 technological prototype**

⁴ *E-mail:* irles@lal.in2p3.fr

⁵ **ABSTRACT:** High precision physics at future colliders as the International Linear Collider (ILC)
⁶ require unprecedented high precision in the determination of the final state of the particles produced
⁷ in the collisions. The needed precision will be achieved thanks to the Particle Flow algorithms (PF)
⁸ which require compact, highly granular and hermetic calorimeters systems. The Silicon-Tungsten
⁹ Electromagnetic Calorimeter (SiW-ECAL) technological prototype design and R&D is oriented
¹⁰ at the baseline design of the ECAL of the International Large Detector (ILD) for the ILC. In this
¹¹ article we present the commissioning and the performance of the prototype in our beam test carried
¹² at DESY in June 2017.

¹³ **KEYWORDS:** Calorimeter methods, calorimeters, Si and pad detectors

14	Contents	
15	1	Introduction
16	2	The SiW-ECAL technological prototype
17	2.1	Silicon sensors
18	2.2	SKIROC: Silicon pin Kalorimeter Integrated ReadOut Chip
19	2.3	Active Sensor Units
20	2.4	Data AcQuisition system
21	2.5	Fully equipped readout modules: the SLABs
22	2.6	The prototype setup
23	3	Commissioning
24	3.1	Tagging and control of the noisy channels.
25	3.2	Optimal trigger threshold determination
26	3.3	S/N ratio in the trigger branch
27	3.4	Prospects
28	4	Performance on positron beam test at DESY
29	4.1	Response to MIP-acting positrons
30	4.1.1	Pedestal and noise determination
31	4.1.2	Energy calibration and tracking efficiency
32	4.1.3	S/N ratio in the charge measurement for MIP interactions
33	4.2	Pedestal and noise stability in a magnetic field
34	4.3	Pedestal stability in electromagnetic shower events
35	5	Summary
36	6	Outlook
37	A	Apéndice: Filtering of fake triggers
18		
19		
20		

38 1 Introduction

39 Future accelerator based particle physics experiments require very precise and detailed reconstruction
40 of the final states produced in the beam collisions. A particular example is the next generation
41 of e^+e^- linear colliders such the ILC[1–5]. This project will provide collisions of polarized beams
42 with centre-of-mass energies (*c.m.e*) of 250 GeV - 1 TeV. These collisions will be studied by two
43 multipurpose detectors: the International Large Detector (ILD) and the Silicon Detector (SiD)[5].
44 To meet the precision levels required by the ILC physics goals, new techniques relying on single

45 particle separation to make possible the choice of the best information available in the full detector
46 to measure the energy of the final state objects have been developed. These techniques are called
47 Particle Flow (PF) techniques [6–8] and allow to reduce the impact of the poor resolution of the
48 calorimeter systems (compared with trackers) in the overall reconstruction. The PF algorithms
49 impose some special requirements in the design of the detectors. For example, it requires highly
50 granular, compact and hermetic calorimeters.

51 The CALICE collaboration is driving most of the efforts on R&D of highly granular calorime-
52 ters [8] for future linear colliders by investigating and building prototypes for several calorimeter
53 concepts. One of these calorimeters is the silicon-tungsten electromagnetic calorimeter, SiW-
54 ECAL. The SiW-ECAL is the baseline choice for the ILD electromagnetic calorimeter. It consists
55 of a detector (in the barrel region) of $24 X_0$ of thickness which corresponds to $\sim 1 \lambda_I$ (interac-
56 tion length). It has silicon (Si) as active material and tungsten (W) as absorber material. The
57 combination of Si and W choices makes possible the design and construction of a very compact
58 calorimeter with highly granular and compact active layers. It will be built an alveolar structure of
59 carbon fiber into which modules made of tungsten plates and the active sensors will be inserted.
60 The very-front-end (VFE) electronics will be embedded in the detector units. The silicon sensors
61 will be segmented in squared cells (or channels) of $5 \times 5 \text{ mm}$: a total of ~ 100 million readout
62 channels will constitute the ECAL for ILD. The desired signal dynamic range in each channel goes
63 from 0.5 MIP to 3000 MIPs. To reduce overall power consumption, the SiW-ECAL will exploit the
64 special bunch structure foreseen for the ILC: the e^+e^- bunches will arrive in spills of $\sim 1\text{-}2 \text{ ms}$
65 width separated by $\sim 200 \text{ ms}$. The data acquisition will be gated during these short windows and
66 during the idle time the bias currents of the electronics will be shut down. This technique is usually
67 denominated power pulsing. In addition to this, to cope with the large amount of channels, the
68 calorimeters should work in self-trigger mode (each channel featuring an internal trigger decision
69 chain) and zero suppression mode.

70 2 The SiW-ECAL technological prototype

71 The first SiW-ECAL prototype was the so called SiW-ECAL physics prototype. It was success-
72 fully tested at DESY, FNAL and CERN running in front of another prototype from the CALICE
73 collaboration, the analogue hadronic calorimeter AHCAL, delivering the proof of concept of the
74 technology and the PF calorimetry. For the physics prototype, the VFE was placed outside the
75 active area with no particular constraints in power consumption. It consisted of 30 layers of Si as
76 active material alternated with tungsten plates as absorber material. The active layers were made of
77 a matrix of 3×3 Si wafers of $500 \mu\text{m}$ thickness. Each of these wafers was segmented in matrices of
78 6×6 squared channels of $1 \times 1 \text{ cm}^2$, allowing for a potential density of 1500 channels/ dm^3 assuming
79 the ILD baseline design constraints on the material repartition and compactness. The prototype
80 was divided in 3 modules of 10 layers with different W depth per layer in each of these modules
81 ($0.4, 1.6$ and $2.4 X_0$) making a total of $24 X_0$. That very first prototype offered a signal over noise
82 on the measured charge of 7.5 for MIP like particles. More results proving the good performance
83 of the technology and the PF can be found in references [9–14].

84 The current prototype is called the SiW-ECAL technological prototype. It addresses the main
85 technological challenges: compactness, power consumption reduction through power pulsing and

86 VFE inside the detector close to real ILD conditions. It will also provide data to deeply study
 87 the PF and provide input to tune simulation programs as for example GEANT4[15–17] which is
 88 widely used in particle physics to simulate the passage of particles through matter. In this section
 89 we described in detail the main features and characteristics of the technological prototype.

90 2.1 Silicon sensors

91 The sensors consist of high resistivity (bigger than $5000 \Omega\text{-cm}$) silicon wafers with a thickness of
 92 $320\mu\text{m}$. The size of the wafers is $9 \times 9 \text{ cm}^2$ and they are each subdivided in an array of 256 PIN
 93 diodes of $5 \times 5 \text{ mm}^2$. A MIP traversing the PIN parallel to its normal will create $\sim 80 h^+e^-$ pairs
 94 per μm which corresponds to 4.1 fC for particles incident perpendicularly to its surface.

95 The original design of the silicon wafers included an edge termination made of floating guard-
 96 rings. It was observed in beam tests [18, 19] that the capacitive coupling between such floating
 97 guard-rings and the channels at the edge created not negligible rates off fake events in tests with
 98 high energy beams (pions and electrons with energies larger than 20-40 GeV) An R&D program
 99 together with Hamamatsu Photonics (HPK Japan) was conducted to study the guard-rings design
 100 as well as the internal crosstalk. It was concluded that using wafers without guard rings and with a
 101 width of the peripheral areas lower than $500\mu\text{m}$ thanks to the use of stealth dicing technique, the
 102 amount of these squared events can be reduced to be at negligible level.

103 For the setup described this article we used different solutions for the edge terminations. For
 104 all of them, the levels of fake events are at negligible level due to the low energy of the beam used
 105 to test the prototype. Therefore, they are not further described here.

106 2.2 SKIROC: Silicon pin Kalorimeter Integrated ReadOut Chip

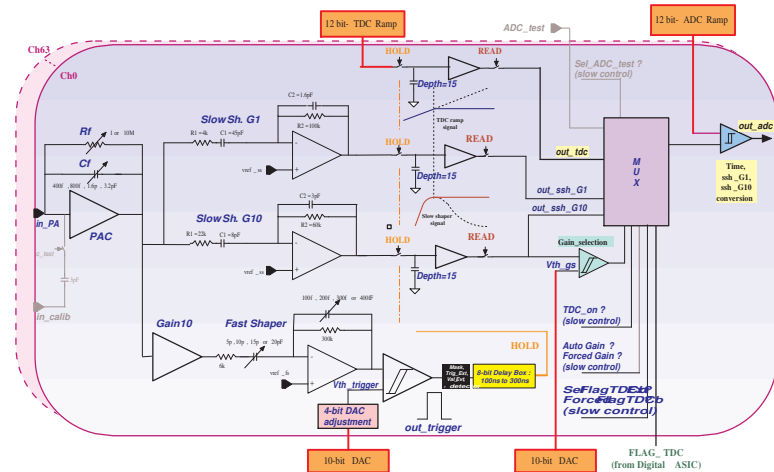


Figure 1. The schematics of the analog part of SKIROC2. High-stack picture (right bottom corner)

107 The SKIROC[20] (Silicon pin Kalorimeter Integrated ReadOut Chip) is a very front end ASIC
 108 (application-specific integrated circuits) designed for the readout of the Silicon PIN diodes. In its
 109 version SKIROC2 it consists of 64 channels in AMS 0.35 μm SiGe technology. A schematic view
 110 of the analog part of the SKIROC2 is shown in Figure 1. Each channel comprises a low noise charge

111 preamplifier of variable gain followed by two branches: a fast shaper for the trigger decision and
112 a set of dual gain slow shaper for charge measurement. The gain can be controlled by modifying
113 the feedback capacitance during the configuration of the detector. With the lowest gain, 6pF, the
114 ASIC will handle a linear dynamic range from 0.1 to up to 1500 MIPs. Finally, a Wilkinson type
115 analogue to digital converter fabricates the digitized charge deposition that can be readout. Once
116 one channel is triggered, the ASIC reads out all 64 channels adding a bit of information to tag
117 them as triggered or not triggered and the information is stored in 15 cell deep physical switched
118 capacitor array (SCA).

119 The SKIROC ASICs can be power-pulsed by taking advantage of the ILC spill structure: the
120 bias currents of the ASIC can be shut down during the idle time between bunch trains. With this
121 method, the ASIC is able to reduce its power consumption down to $25 \mu\text{W}$ per channel, meeting
122 the ILC requirements. The power pulsing feature is used for all the results discussed in this paper
123 and for first time in long periods of data taking in beam test.

124 **2.3 Active Sensor Units**

125 The entity of sensors, thin PCB (printed circuit boards) and ASICs is called Active Signal Units or
126 ASU. An individual ASU has a lateral dimension of $18 \times 18 \text{ cm}^2$. The ASUs are currently equipped
127 further with 16 SKIROC2 ASICs for the read out and features 1024 square pads (64 per ASIC) of
128 $5 \times 5 \text{ mm}$. The channels and ASICs are distributed along the ASU as shown in Figure 2. Each ASU
129 is equipped with 4 silicon wafers as the described in Section 2.1. The high voltage is delivered to
130 the wafers using a HV-kapton sheet that covers the full extension of the wafers.

131 Current version of the PCB is called the FEV11. It has a thickness of 1.6mm and 2.7mm
132 if we include on top the ASICs in its current packaging (1.1 mm thick LFBGA package). With
133 these characteristics, a potential density of 3800 channels/ dm^3 is achievable keeping the space and
134 interaction length requirements of the the baseline design of the ECAL forthe ILD. This number
135 should be compared with the density achieved in beam tests with the physics prototype: 1500
136 channels/ dm^3 . With the first versions of the technollogical prototype we reached similar potential
137 density level as in the current version but equipping only a quarter of the ASUs surface [24].

138 **2.4 Data AcQuisition system**

139 The subsequent chain of the data acquisition (DAQ)[21] system consists of three components,
140 enumerate from upstream to downstream from the data flow perspective:

- 141 1. The first component is the so called detector interface (DIF) which is placed at the beginning
142 of each layer holding up to 15 ASUs.
- 143 2. All DIFs are connected by single HDMI cables to the concentrator cards as the second
144 component: the Gigabit Concentrator Cards (GDCCs). These cards are used to control up to
145 7 DIFs. They collect all data from the DIFs and distribute among them the system clock and
146 fast commands.
- 147 3. The most downstream component, is the clock and control card (CCC) which provides a
148 clock, control fan-out of up to 8 GDCCs and accepts and distributes external signals (i.e.
149 signals generated external pulse generator to simulate the ILC spill conditions).

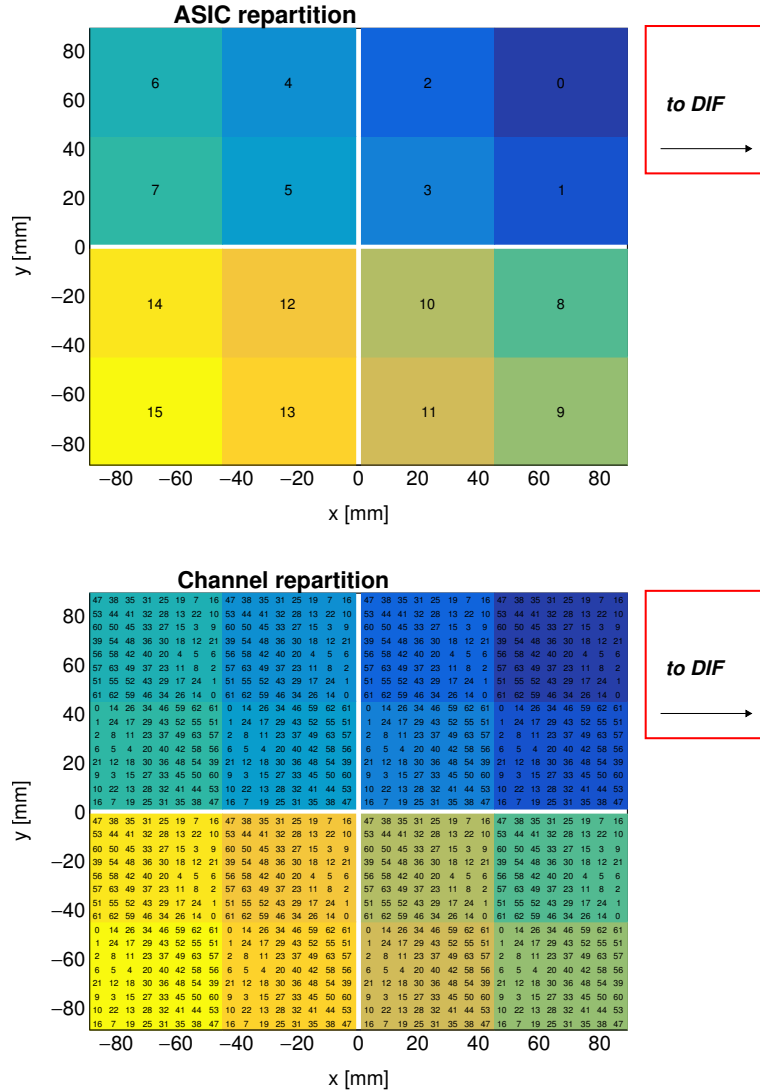


Figure 2. Repartition of the ASIC (up) and channels (down) in one ASU. In this perspective, the Si-Sensors are glued in the back. The channels are separated (in x and y) by 5.5 mm. The empty cross in the middle of the ASU corresponds to the 1 mm separation between the sensors. The areas covered by the different ASICs and channels are labeled with numbers following design and DAQ criteria: from 0-16 in the case of the ASICs and from 0-63 in the case of the channels.

150 The whole system is controlled by the Calicoes and the Pyrame DAQ software version 3 [22, 23].

151 2.5 Fully equipped readout modules: the SLABs

152 A full equipped readout module is shown in Fig. 3. These modules are called SLABs and consist
 153 of a chain of one or several fully equipped ASUs connected to a data acquisition system (DAQ)
 154 through an adapter board, called SMBv4. The SMBv4 also serves as to hold other services as power
 155 connectors or the super capacitances used for the power pulsing. These capacitances of 400mF with
 156 16 mΩ of equivalent serial resistance. The capacitances are extra dimensioned to provide enough



Figure 3. Open single SLAB with FEV11 ASU, 16 SKIROC 2 and the interface card visibles.

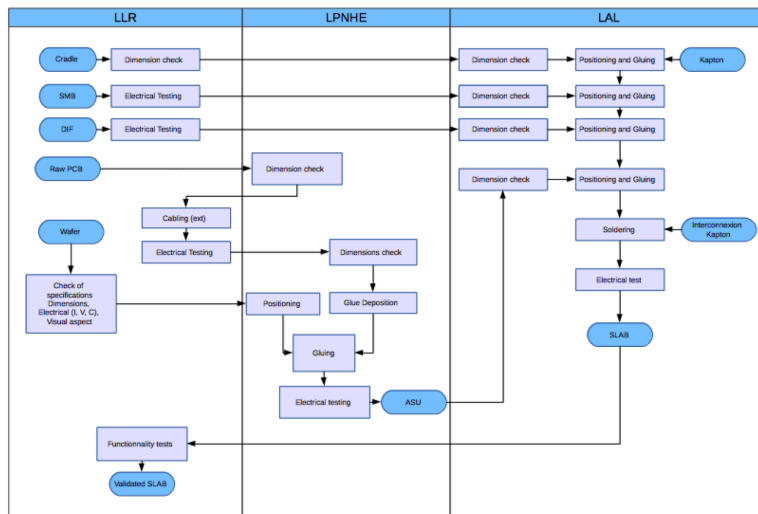


Figure 4. Process flow for the assembly of the SiW-ECAL SLABS.

157 local storage of power to assure stable low voltage levels during the power pulsing. The readout
 158 modules are embedded on a "U" shape carbon structure to protect the wafers. The full system is
 159 then covered by two aluminum plates to provide electromagnetic shielding and mechanical stability.

160 For the production of the small sample of SLABs studied in this document, a scalable working
 161 procedure has been established among several groups [25] profiting from the funding of projects like
 162 AIDA2020 or the HIGHTEC emblematic project of the P2IO. A schematic view of this assembly
 163 procedure chain can be seen in Figure 4. For more details we refer to Ref.[25]. This process is to
 164 be extrapolated to a full assembly procedure for e.g. the ILD detector.

165 **2.6 The prototype setup**

166 A photograph showing the SiW-ECAL technological prototype setup can be seen in Figure 5.
167 Current prototype consists on 7 layers of SLABs housed by a PVC and aluminum structure that
168 can hold up to 10, in slots separated by 15mm each. The first six layers were placed in the first
169 six slots and the last one was in the last slot. In the following sections, we will refer to layers
170 number 1 to 7, where the 1 is the closest to the beam pipe and 7 is the farthest. This setup is used
171 for commissioning (Section 3) and for the beam test (Section 4). In both cases, the detector was
172 running in power pulsing mode.

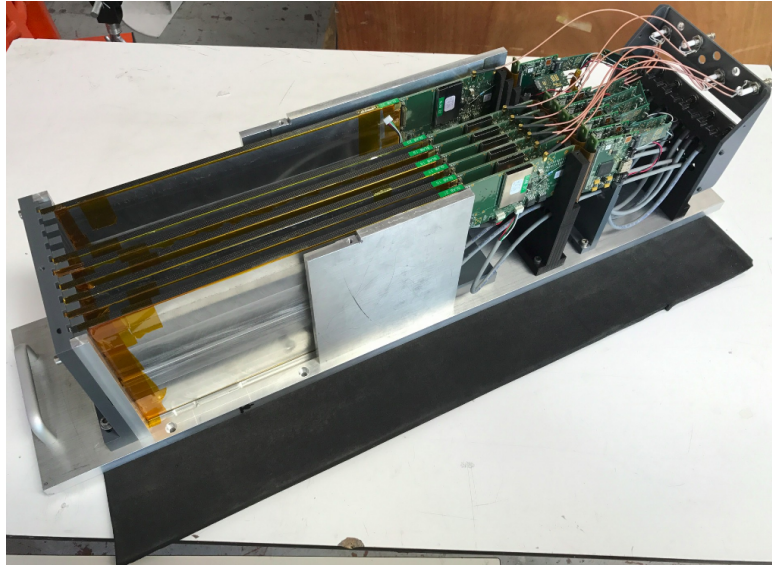


Figure 5. Prototype with 7 layers inside the aluminum stack.

173 **3 Commissioning**

174 This beam test was prepared by a commissioning phase comprising the debug of the short SLABSs
175 with special emphasis in the control of the noise and the study of the prototype performance in
176 cosmic ray tests.

177 Earlier experiences with the SKIROC2 ASIC are reported in Refs. [24, 26]). Internal SKIROC2
178 parameters reported in these references are adopted in the following unless stated otherwise. For
179 example, a gain value of 1.2pF for the preamplifier is used. With this gain, the SKIROC2 features a
180 linearity better than 90% for 0.5-200 MIPs, which is sufficient for electromagnetic showers created
181 by few GeV electrons or positrons.

182 The main goal of the the commissioning procedure is the optimization of the trigger thresholds
183 to levels in which we are able to record physics signals bellow the MIP level without saturating our
184 DAQ with noise signals. This requires a careful and systematic procedure to:

- 185 1. identify the readout channels that are noisy in high trigger threshold above MIP signal
186 conditions

187 2. and select the optimal trigger threshold levels.

188 During the commissioning, we observed the repetition of coherent noise events affecting to
189 several SLABs at the end of acquisitions with long gating time. The situation could be remedied
190 by improving the isolation of the individual SLABs and by reducing the data taking to short gating
191 times.

192 All runs dedicated to the commissioning were characterized by:

- 193 • their short gating windows for the acquisition (1-2ms) at low repetition frequencies (1-5 Hz)
194 to minimize the chances of having real events due to cosmic rays during the data taking and
195 the coherent noise events due to grounding issues;
- 196 • and the relatively high trigger threshold values between 400 and 250 DAC (which are equiv-
197 alent to ~ 2 and ~ 0.5 MIP respectively, see Section 3.2 for more information).

198 3.1 Tagging and control of the noisy channels.

199 We found two different types of noisy channels. One set consists of channels randomly distributed
200 along the surface of every ASU and the other consists of channels systematically noisy in all the
201 ASUs. Preliminary inspections of the PCB layout hint that the channels in the latter set are noisy due
202 to improvable routing of the PCB. Deeper studies on the PCB routing must be conducted to clarify
203 this. All the noisy channels have been identified and masked and the power of their preamplifiers
204 has been disabled. All the results shown in the following sections are obtained in these conditions.

205 The list of the noisy channels was obtained by means of dedicated data taking runs. In these
206 runs we scan trigger thresholds and progressively mask channels that exhibit counts. In each step,
207 the decision of tagging a channel as noisy was taken following the next rules:

- 208 • if the channel was triggered at rates larger than 0.5-1% of the total number of triggers per
209 ASIC it was added to the list;
- 210 • if a channel was tagged as noisy in at least three of the SLABs, it was tagged as noisy for all
211 and added to the list of channels being suspect of suffer from routing issues.

212 In addition to the different noisy channel types described above, we also have masked full
213 sectors of the SLABs if an ASIC was faulty (at least 70% of channels listed as noisy) or if a Si-wafer
214 was damaged (high leakage currents). The results of this study is summarized in Figure 6.

215 3.2 Optimal trigger threshold determination

216 After the noisy channels have been masked, dedicated trigger threshold scan runs are taken, and
217 the results are shown in threshold scan curves where the x-axis represents the threshold value¹
218 and the y-axis the number of recorded signals normalized to 1. In the absence of external signals
219 (cosmic rays, injected signals, etc) the falling edge position in the threshold scan curves is due to
220 the electronic noise at the output of the fast shaper (the trigger decision branch on the SKIROC)

¹The threshold values are given in internal DAC units which are translated to meaningful physical quantities in Section 3.3.

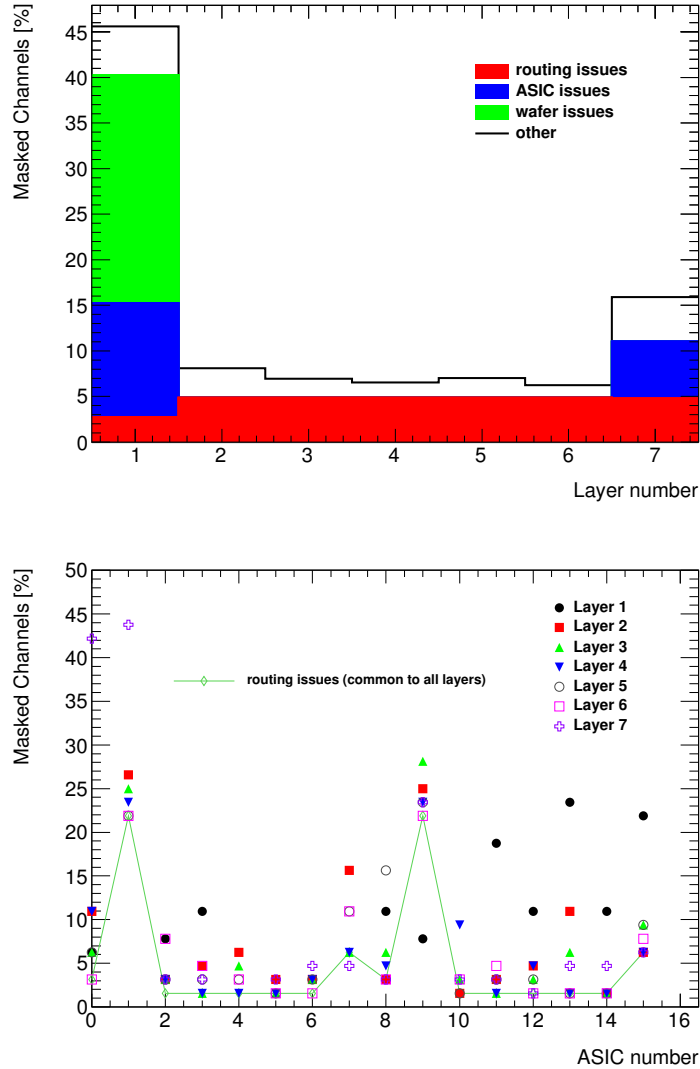


Figure 6. Fraction of channels that are tagged as noisy in all slabs. Top: inventory of the different type of noisy channels per slab. Bottom: break down of the total number of noisy channels per ASIC. The ASICs 4-7 (wafer issue) and 10 from layer 1 and the ASIC 4 from layer 7 are not included in the second plot since they are fully masked.

and it depends on the slow clock frequency. These threshold scan curves are approximated by a complementary error function:

$$\frac{2p_0}{\sqrt{\pi}} \int_{\frac{DAC-p_1}{p_2}}^{\infty} e^{-t^2} dt, \quad (3.1)$$

where p_0 is 1/2 of the normalization, p_1 is the value in which the noise levels are the 50% of its maximum and p_2 give us the width of the ThS curve.

In Figure 7 two threshold scans curves are shown together with the fit by the theoretical function for two different channels from the second layer of the setup are shown.

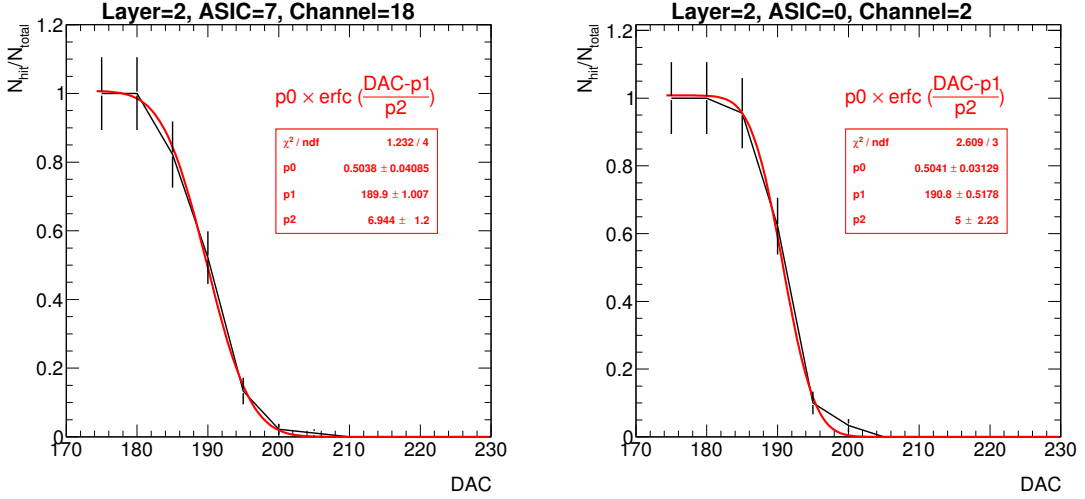


Figure 7. Two threshold scan curves.

For every ASICs, after performing the fit of the theoretical curves to the threshold scans, the average values of the p_1 and p_2 are calculated. These are represented by $\langle p_{1,2}^{\text{ASIC}} \rangle$ in the following. The final threshold value of every ASIC, in DAC units, was chosen using the following formula

$$DAC_{\text{optimal}}^{\text{ASIC}} = \text{maximum}(\langle p_1^{\text{ASIC}} \rangle + 5 \times \langle p_2^{\text{ASIC}} \rangle, 230). \quad (3.2)$$

This formula was applied if at least the 30% of the 64 channels in the ASIC could be fitted. If not, a global DAC value of 250 was set.

The optimal trigger threshold values for all ASICs are shown in Figure 10, in internal DAC units and in MIPs. In the next section we explain how the conversion is done.

3.3 S/N ratio in the trigger branch

Performing threshold scan scurves using real signals allow to calculate the signal over noise (S/N) ratio to trigger. For that we compare the curves for 1 MIP and 2 MIP injected signals. The S/N is, therefore, defined as the ratio between the distance of both curves at its 50% and the width of the curves. In Figure 8 we see the 1 MIP and 2 MIP curves obtained for several channel in a SKIROC testboard in which a single SKIROC2 in BGA package is placed and the 1 MIP and 2 MIPs signals are directly injected in the preamplifier (via a 3 pF capacitor located in the injection line as shown in Figure 1).

We have obtained similar results using real signals, in this case cosmic rays signals. This is shown in Figure 9 where we show the result of the fit to the threshold scan curves cosmic rays integrated for all channels in one ASIC. For completeness, the fit of threshold scan curves for all channels in the same ASIC are also shown.

From these two results we extract the value of

$$S/N = 12.9 \pm 3.4 \quad (3.3)$$

for the trigger branch. The central value is calculated from the comparison of the blue and red curves in Figure 1 and using the width of the 1 MIP curve in the denominator. The estimated uncertainty

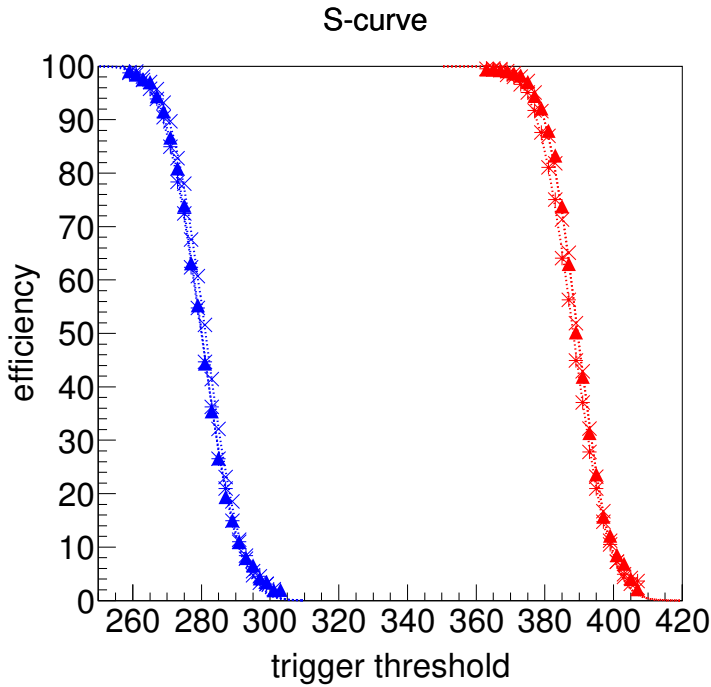


Figure 8. Threshold scan curves with charge injection (1 MIP in blue and 2 MIPs in red) for two different channels in a SKIROC2 testboard.

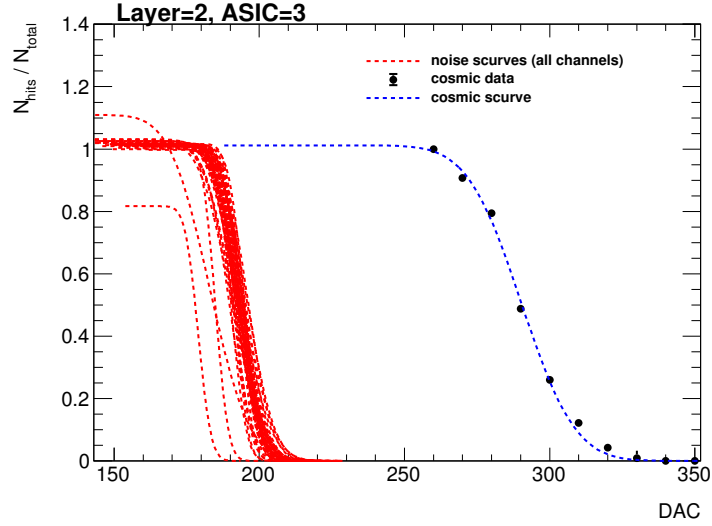


Figure 9. Threshold scan curves for noise (channel by channel, only the result of the fit) and cosmic rays (all channels together) for one ASIC in layer 2.

249 has two components: the difference of width between the 1 and 2 MIP curves of injected signals
 250 and the differences (width and middle point) between the 1 MIP curves for injected and cosmic ray
 251 signals.

252 Dedicated studies in beam test are needed in order to reduce the uncertainty of this measurement.

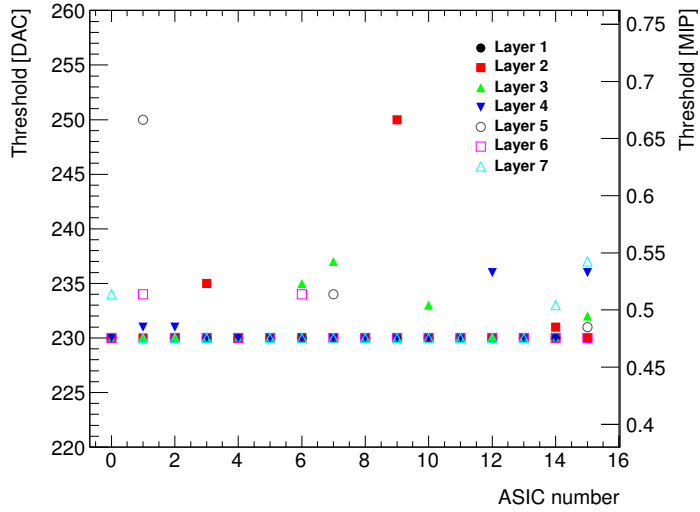


Figure 10. Summary of the trigger threshold settings in internal DAC units and in MIP units.

253 However, by combining the information contained in the Figs 8 and 9, we can also estimate the
 254 energy that corresponds to a given trigger threshold. This is shown in Figure 10, where the chosen
 255 thresholds of every ASIC being tested in beam are shown.

256 3.4 Prospects

257 The commissioning procedure described above relies on very conservative decisions due to the
 258 presence of unknown noise sources during largest of the commissioning phase. These sources
 259 are now well known and therefore a new “noise commissioning procedure” has been studied. It
 260 will consist on an iterative algorithm that first will identify and mask the channels in which the
 261 number of triggers per channel will be compared with the number of expected triggers assuming
 262 only cosmic rays as signal. This will allow us to have a definition of the noise levels for each
 263 channel independently instead of relative to the total number of triggers recorded by the ASIC.
 264 Finally, once the noisy channels are identified, the threshold are further optimized with a last run
 265 for the identification of the residual noisy channels.

266 Using this new procedure we manage to reduce the number of masked channels by a factor of
 267 two without any loss of performance, at least in the laboratory and using 3 of the 7 SLABs. This new
 268 procedure will also be applied in the next beam test. Also, in order to optimize the commissioning
 269 of the detector, we propose a new set of measurements in the next beam test such as a threshold
 270 scan for the determination of the S/N in the trigger line. The later can be done by the comparison of
 271 threshold curves taken with incident MIP-acting particles and MIP-acting particles traversing the
 272 detector tilted by 45 degrees with respect to the beam direction.

273 4 Performance on positron beam test at DESY

274 The beam test line at DESY provides continuous positron beams in the energy range of 1 to 6 GeV
 275 with rates from few hundreds of Hz to few KHz with a maximum of ~ 3 KHz for 2-3 GeV. The

276 particles beam ies produced as follows: first, the electron/positron synchrotron DORIS II is used to
277 produced a photon beam via bremsstrahlung when interacting with a carbon fiber target; secondly,
278 these photons are then converted to electron/positron pairs; and, finally, the beam energy is selected
279 with dipole magnets and collimators. In addition, DESY gives acces to a bore 1 T solenoid, the
280 PCMag.

281 The physics program of the beam test can be summarized in the following points:

- 282 1. Calibration without tungsten absorber using 3 GeV positrons acting as minimum ionizing
283 particle (MIPs) directed to 81 position equally distributed over the modules.
- 284 2. Test in magnetic field up to 1 T using the PCMag. For this test a special PVC structure was
285 designed and produced to support one single SLAB. The purpose of such test was twofold:
286 first to prove that the DAQ, all electronic devices and the mechanical consistency of the SLAB
287 itself are able to handle strong magnetic fields; second to check the quality of the data and
288 the performance of the detector during the data taking when running in a magnetic field.
- 289 3. Response to electrons of different energies with fully equipped detector, i.e. sensitive parts
290 and W absorber, with three different repartitions of the absorber material:
 - 291 • W-configuration 1: 0.6, 1.2, 1.8, 2.4, 3.6, 4.8 and 6.6 X_0
 - 292 • W-configuration 2: 1.2, 1.8, 2.4, 3.6, 4.8, 6.6 and 8.4 X_0
 - 293 • W-configuration 3: 1.8, 2.4, 3.6, 4.8, 6.6, 8.4 and 10.2 X_0

294 First reports on this beam test can be find in Refs. [27, 28]. In this paper we discuss in more
295 detail the results of the pedestal, noise and MIP calibration in Section 4.1. We show also results on
296 the pedestal and noise stability when running inside a magnetic field in Section ???. Finally, a first
297 peek to the response and stability of the detector in electromagnetic showers events is discussed in
298 Section 4.3.

299 4.1 Response to MIP-acting positrons

300 The calibration runs have been used to calculate the pedestal distribution reference values and the
301 noise levels (the width of the pedestal distrution) of each channel. In Figure 11 we show the signal
302 and pedestal distribution of a single channel after subtracting the pedestal mean position. The
303 results of the MIP calibration fit are shown in red (see Section 4.1.2 for more details) The pedestal
304 distribution is shown only for the first SCA to keep the y-axis within a reasonable range. The signal
305 distribution is integrated over all SCAs.

306 4.1.1 Pedestal and noise determination

307 The pedestal is calculated as the mean position of the ADC distribution of channels without trigger.
308 The noise is associated to the width of such distribution. The pedestal correction is done layer-,
309 chip-, channel- and SCA-wisely due to the large spread of values between pedestals, as observed
310 in Figure 12 (left plot) and Figure 13 (also left plot). For the noise, the dispersion is much smaller
311 ($\sim 5\%$). This is shown in the right plots of Figures 12 and 13. From now on, the pedestal correction
312 is applied to all the results presented.

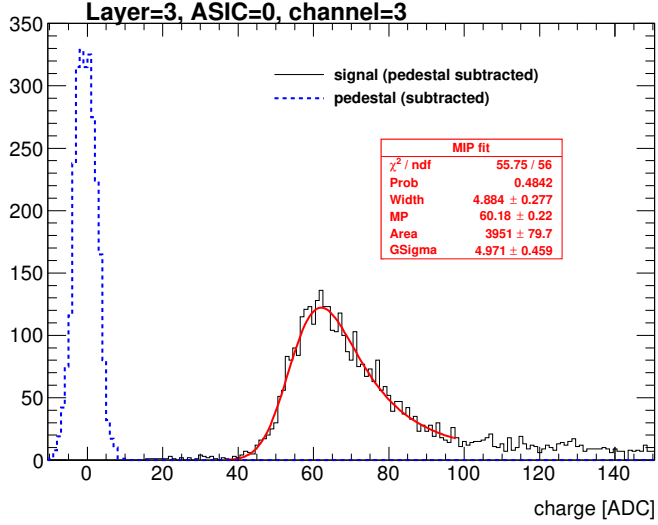


Figure 11. Pedestal (blue dashed line) and signal (black continuous line) distribution for one channel in the third layer.

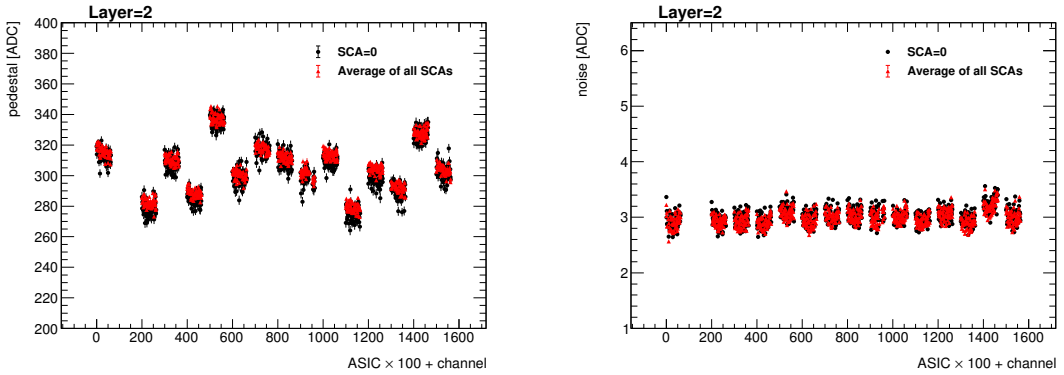


Figure 12. Pedestal mean position (upper plot) and width (lower plot) for all channels in one layer. The data is grouped on bunches in which the value in the x-axis corresponds to the value of the channel number plus the value of the ASIC number multiplied by 100. The black points show the value for the first SCA and the red points show the average value for all the others SCAs (with the standard deviation of the sample as error bar).

4.1.2 Energy calibration and tracking efficiency

After the pedestals are calculated and subtracted to the hit distributions, those are fit by a Landau function convoluted with a Gaussian. The most-probable-value of the convoluted function is taken as the MIP value, allowing thus for a direct conversion from ADC units to energy in MIP units. We have obtained a raw energy calibration spread of the 5% among all channels with the 98% of all available channels being fitted. Results are summarized in figure 14, leftmost plot.

We checked the MIP calibration in all calibrated channels by selecting tracks incident perpendicular to the layers surface. The results are shown in figure 15 where the single channel energy distribution for MIPs is shown for all calibrated channels in the same distribution. The maximum

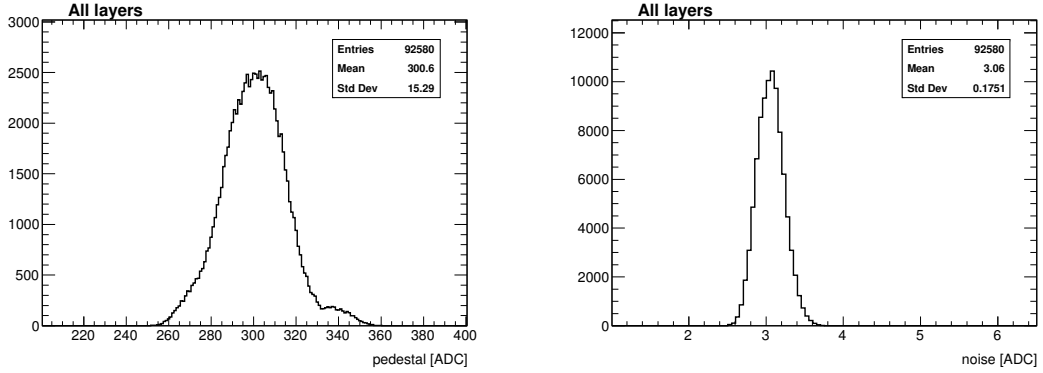


Figure 13. Pedestal mean position (left) and width (right) for all channels and all SCAs in the setup.

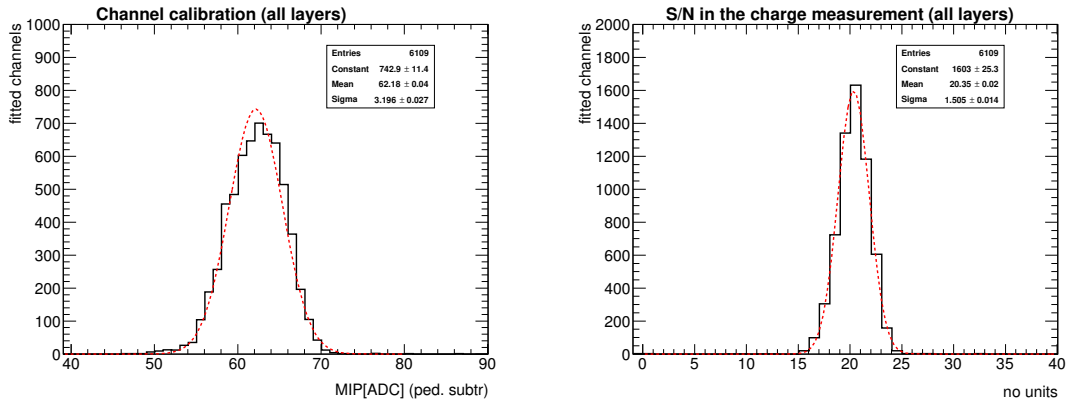


Figure 14. Result of the MIP position calculation and signal over noise calculation for all calibrated channels.

peaks at 1 MIP as expected after a good calibration. In addition to this, a second and a third peak appear visible. These peaks are due to events involving multiple particles crossing the detector.

To evaluate the single hit detection efficiency we define a high purity sample of events by selecting tracks with at least 4 layers with a hit in exactly the same channel. Afterwards we check if the other layers have or not a hit in the same channel (expanding the search to the closest neighbouring channels) with energy larger or equal than 0.3 MIP. Finally, we repeat this for all layers and channels. The results are shown in Figure 16. Except few exceptions, the efficiency is compatible with 100%. Lower efficiencies in the first layer are related to the presence of noisy channels not spotted during the commissioning. In the last layer (separated from the other layers by four slots of 1.5 cm instead of only one) we also observe few small deviations from the $\sim 100\%$ which are indeed associated to a slight misalignment of the detector. If we remove these channels from the analysis the full efficiency is recovered.

4.1.3 S/N ratio in the charge measurement for MIP interactions

The signal-over-noise ratio in the charge measurement (corresponding to the slow shaper of the SKIROC2) is defined as the ratio between the most-probable-value of the Landau-gauss function fit to the data (pedestal subtracted) and the noise (the pedestal width). This quantity has been

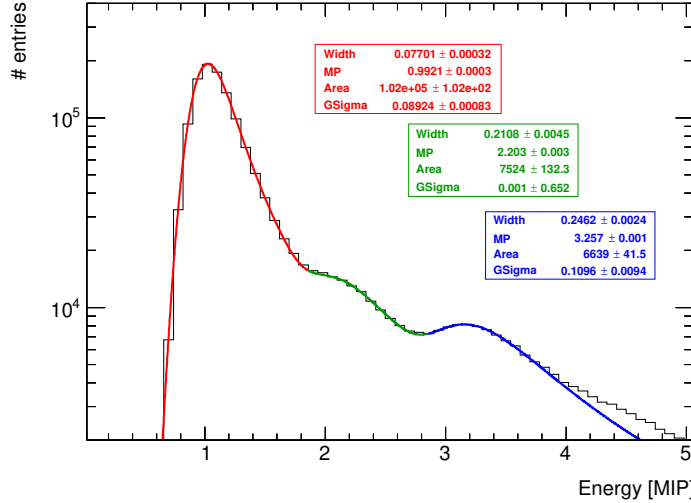


Figure 15. Energy distribution for all calibrated channels when selecting tracks of 3 GeV positron acting as MIPs.

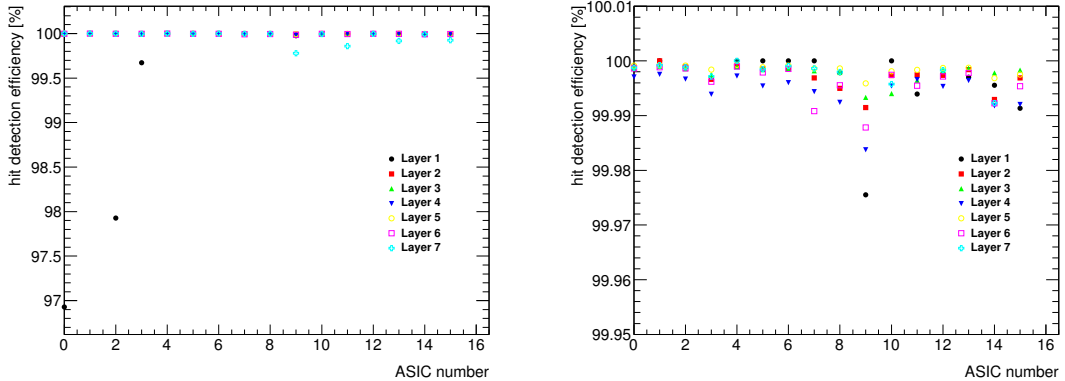


Figure 16. Left: MIP detection efficiency for all layers and ASICs in high purity samples of tracks of MIP-like acting particles. Right: same figures with a zoom in the y-axis. In both cases, the average efficiency of the 64 channels in each ASIC is shown.

338 calculated for all channels and all layers. The average S/N is to 20.4. Results are summarized in
 339 Figure 14, rightmost plot.

340 4.2 Pedestal and noise stability in a magnetic field

341 The data taking inside the magnetic field has been divided in three steps: a) a with a magnetic field
 342 of 1 T; b) a run with 0.5 T; c) a final run with the magnet off. The beam, 3 GeV positrons, was
 343 hitting in the area of the PCB readout by the ASIC number 12.

344 The pedestal positions and noise levels of the channels of the ASIC 12 when the SLAB
 345 is inside of the PCMag are compared with the results from the calibration run described in the
 346 previous section. This is shown in Figure 17. We see that the agreement is perfect within the

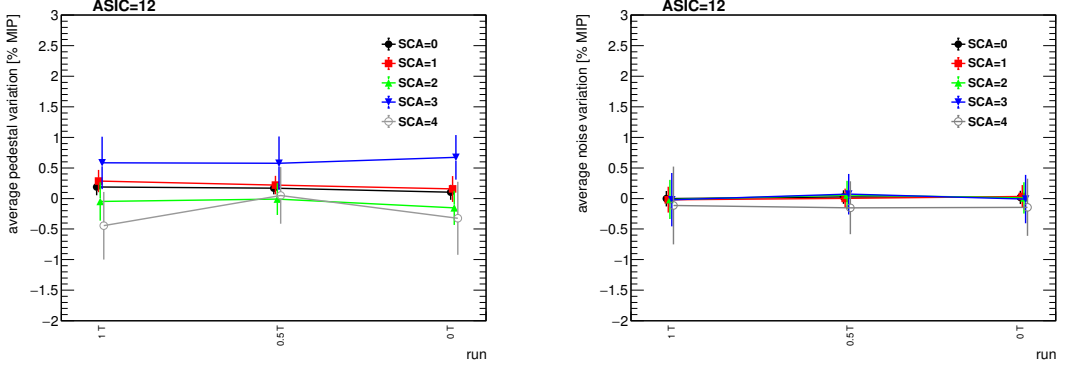


Figure 17. Average deviation of the pedestal mean position (left) and width (right) for all channels in the ASIC 12.

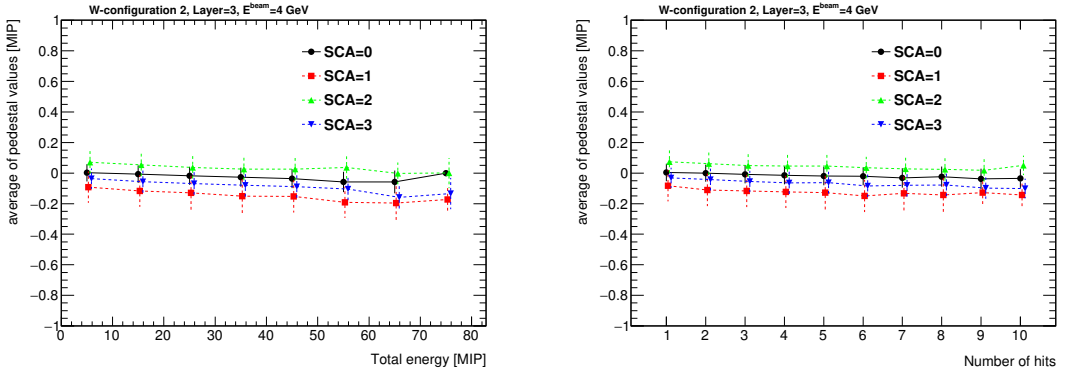


Figure 18. Left: mean position of the projection of the pedestal distribution of all channels calculated when different energies are collected in the ASIC (in bins of 10 MIPs). Right: same but as a function of the number of hits. In both cases, the results are shown for few SCAs. The points for the curves with SCA larger than zero are slightly shifted in the x-axis to optimize the visualization.

statistical uncertainties. Due to the lower rates in this beam area, the analysis is only done up to few SCAs.

4.3 Pedestal stability in electromagnetic shower events

In this section we discuss the pedestal stability in events with large amount of charge collected by the ASICs, as are the electromagnetic shower events. All the results shown in this section correspond to data taken during the tungsten program, using the W-configuration number 2 when shooting the beam in the area registered by the ASIC 12 (and partially in the 13). Only information recorded by ASIC 12 is used in the analysis. For other configurations we get comparable results. In order to select a high purity of electromagnetic shower like the events, we used a simple criteria: select only events with at least 6 of the layers with at least a hit with $E > 0.5$ MIP.

Two main observations have been extracted from the recalculation of the pedestals and its comparison with the values obtained previously during the calibration runs. The first observation consists in a relatively small drift of the pedestal values towards lower values when the collected

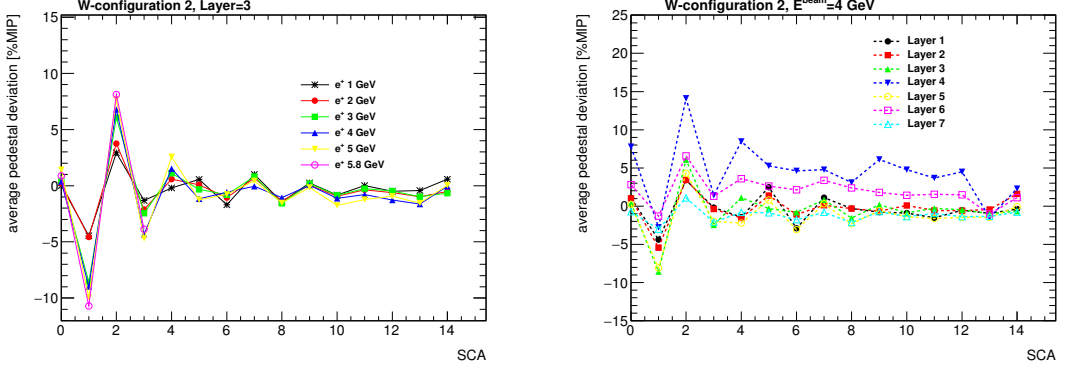


Figure 19. Left: average value on each SCA of the calculated pedestals for all channels of ASIC 12 in the Layer 3 for different energies of the beam. Right: same but fixing the energy of the beam and comparing several layers.

energy is high (or when the number of triggered channels is large). This is shown in Figure 18 for several SCAs where the average of the projection of the pedestal distribution for all channels non triggered in ASIC 12 of layer 3 is plot as a function of the total energy measured by the ASIC (or the total number of hits). We see that in both cases, the shapes of the curves for each SCA are very similar. This feature is known and it is due to the architecture of the SKIROC2 ASICs where high inrush of currents can slightly shift the baseline of the analogue power supply.

The second observation extracted from this analysis can be also seen in Figure 18 but more clearly in Figure 19: in addition to the small drift of the pedestal value an SCA-alternate global shift is observed. We see that the effect is enhanced when large amounts of charge are deposited in the ASIC (*i.e.* at larger beam energies or for the layers in the maximum of the shower profile). We also observed that this alternation is only SCA dependent and does not depends on the time in which the deposit of energy occurs within the acquisition. This is not yet fully understood although the fact that the effect is observed in alternate SCAs hints that something is affecting to the digital part of the ASIC (where the SCAs enter in play). Dedicated tests in the laboratory and in the beam are needed in order to clarify this issue.

5 Summary

The R&D program of the highly granular SiW-ECAL detector is in an exciting phase. After the proof of principle of the imaging calorimetry concept using the physics prototype, the technological prototype is being constructed and tested. In this document we describe the commissioning and beam test performance of a prototype built in with the first fully assembled detector elements, in contrast with previous beam tests. In addition, with the setup used in this beam test we reached levels of granularity similar to the targets of the ILD detector for the ILC. This is also the first time that a SiW-ECAL prototype continuously takes data in a beam test running in power pulsing mode, one of the crucial features for the detectors for the ILC. Finally, we tested the performance of the detector modules working for long periods inside magnetic fields.

385 A very comprehensive and detailed commissioning procedure has been established and opti-
386 mized allowing us to identify and isolate the different noise sources that could spoil the data taking.
387 The beam test has provided a lot of useful data to study the performance of the detector and to
388 perform a channel by channel calibration, showing a good homogeneity with a spread of the 5% for
389 all channels. The signal over noise of the detector has been evaluated to be 12.8 for the trigger
390 decision and 20.4 for the charge measurement using, in both cases, MIP signals as reference.

391 6 Outlook

392 In parallel to the work described here, several R&D efforts are being carried. One of these efforts
393 is directed to the design and test of new ASICs. In fact, a new generation of SKIROC2, the 2a,
394 has been delivered and it is being tested in the dedicated testboards and it has been integrated in
395 new ASUs. In addition, a new generation of the ASIC, SKIROC3, is foreseen for the final detector
396 construction. In contrast with SKIROC2/2a, the new ASIC will be fully optimized for ILC operation,
397 *i.e.* full zero suppression, reduced power consumption etc.

398 Many efforts are also concentrated in the construction and test of long SLABs made of several
399 ASUs enchain since we know that the ILD ECAL will host long layers of up to \sim 2.5m. This
400 device constitutes a technological challenge in both aspects, the mechanical (very thin and long
401 structure with fragile sensors in the bottom, complicated assembly procedure...) and the electrical
402 (*i.e.* transmission of signals and high currents). For example, interconnections between ASUs and
403 between ASU and interface card are one of the most involved parts of the assembly and require
404 close collaboration between mechanical and electronic engineers. The construction and test of a
405 long SLAB prototype of \sim 8 ASUs is currently ongoing.

406 In parallel, a different proposal for a thinner ASU design is being investigated. This is motivated
407 by the high density of channels demanded by the Particle Flow algorithms. In this alternative PCB
408 design the ASICs are directly placed on board of the PCB in dedicated cavities. The ASICs will be
409 in semiconductor packaging and wire bonded to the PCB. This is the so-called COB (chip-on-board)
410 version of the ASU. A small sample of FEV11_COBs (same connexion pattern with the interface
411 card than FEV11) with a total thickness of 1.2 mm (to be compared with the 2.7 of the LFBGA
412 solution) has been produced and tested in the laboratory showing its readiness for tests with particle
413 beams. A sample can be seen in Figure 20. These new boards maximize the density of channels
414 (6000 channels/dm³) for the ECAL of the ILD and will allow to satisfy the baseline requirements
415 of the ECAL for the ILD.

416 Finally, intensive R&D on the compactification of the DAQ towards meeting the ILD tight
417 space requirements is being done by the SiW-ECAL collaboration.

418 It is foreseen that all these developments, with the exception of the SKIROC3, will be tested
419 with particle beams during 2018-2019.

420 Acknowledgments

421 This project has received funding from the European Union's Horizon 2020 Research and Innovation
422 program under Grant Agreement no. 654168. This work was supported by the P2IO LabEx (ANR-
423 10-LABX-0038), excellence project HIGHTEC, in the framework 'Investissements d'Avenir' (ANR-

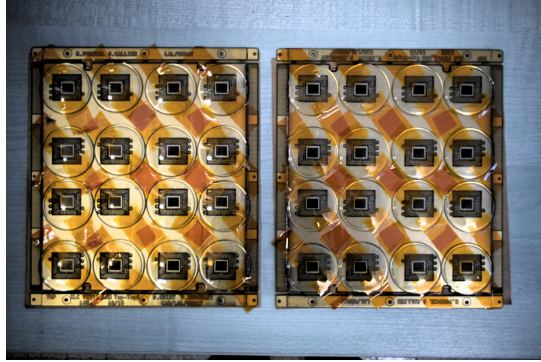


Figure 20. Two FEV11_COB boards with 16 SKIROC2a wire bonded. The ASICs are protected with watch glasses.

424 11-IDEX-0003-01) managed by the French National Research Agency (ANR). The research leading
 425 to these results has received funding from the People Programme (Marie Curie Actions) of the
 426 European Union's Seventh Framework Programme (FP7/2007-2013) under REA grant agreement,
 427 PCOFUND-GA-2013-609102, through the PRESTIGE programme coordinated by Campus France.
 428 The measurements leading to these results have been performed at the Test Beam Facility at DESY
 429 Hamburg (Germany), a member of the Helmholtz Association (HGF).

430 A Apéndix: Filtering of fake triggers

431 Several types of fake signals have been observed in the technological prototype since its construction
 432 and test. A detailed description of them can be found in previous articles, as for example, in Ref.
 433 [24]. All these fake signals are easily identified and tagged during the data acquisition and removed
 434 afterwards from the analysis not introducing any significance loss of performance as can be seen,
 435 for example, in the hit detection efficiency plots (see Section 4.1.2). In the following, we briefly
 436 describe the status of the monitoring, debugging and filtering of such kind of events.

437 Empty triggers

438 Empty trigger events are a well known feature of SKIROC2. The SKIROC2 uses an OR64 signal
 439 to mark the change to a new SCA when a signal over threshold is detected. The empty triggers
 440 appear when during the acquisition the rising edge of the slow clock falls during the OR64 signal
 441 and therefore the change to a new SCA is validated twice. This effect creates around 17% of empty
 442 events which are easily filter and removed from the analysis. The ratio of empty triggers in the new
 443 SKIROC2a has been reduced to the $\sim 2 - 3\%$.

444 Plane events and retriggers

445 Another well known issue is the appearance of bunches of consecutive fake triggers, called retriggers,
 446 that saturates the DAQ. Although the ultimate reason of the appearance of these events remains not
 447 clear, it is suspected that they are related to distortions of the power supply baselines. We know
 448 that the SKIROC2 and 2a preamplifiers are referenced to the analog power supply level, therefore,
 449 any voltage dip can be seen as signal by the preamplifiers. Moreover the presence of a high inrush

450 of current due to many channels triggered at the same time can create these voltage dips and also
451 produce the so called plane events (most of the channels triggered at once). In previous studies (*i.e.*
452 reference [24]), the ratio of retriggers and plane events was reduced by improving the power supply
453 stabilization capacitances. It is important to remark that all layers and all ASICs analog and digital
454 levels are powered using the same power supply. Moreover, the high voltage power supply for the
455 polarization of the PIN diode is also common for all layers and the grounding levels of the low
456 and high voltages supplied are shared within the slab. Therefore any noise in these power supplies
457 or any overload of an ASIC may participate in the creation of fake signals in different ASICs and
458 layers.

459 Studying the MIP calibration data of this beam test we have noticed that the concentration of
460 the retriggers and plane events in ASICs far from the beam spot is higher than in the ASICs that
461 are reading out the information of real hits. Even more, this concentration is even higher near the
462 channels 37 and the channels masked as suspicious of suffering from routing issues. The ratio these
463 events have been estimated to be of 1 – 3% in the ASICs where high frequency interactions are
464 produced (*i.e.* using 3 GeV positrons ate 2-3 KHz) and at higher rates even larger than 40% in other
465 ASICs far from the beam spot. Moreover, it has been noticed a correlation between the time that
466 an ASIC was full and the time of the appearance of some retriggers in other areas of the PCB. This
467 correlation corresponds to $\sim 1.6 \mu\text{s}$ which hints of a distortion on the analogue power supply when
468 the signal that informs the DIF that one ASIC memory is full is transmitted through the PCB.

469 We should point out that these events are easily filtered out during the analysis (or even during
470 the online monitoring) and that no impact is observed in the data, *i.e.* in the MIP detection efficiency.

471 References

- 472 [1] T. Behnke, J. E. Brau, B. Foster, J. Fuster, M. Harrison, J. M. Paterson et al., *The International Linear
473 Collider Technical Design Report - Volume 1: Executive Summary*, [1306.6327](#).
- 474 [2] H. Baer, T. Barklow, K. Fujii, Y. Gao, A. Hoang, S. Kanemura et al., *The International Linear
475 Collider Technical Design Report - Volume 2: Physics*, [1306.6352](#).
- 476 [3] C. Adolphsen, M. Barone, B. Barish, K. Buesser, P. Burrows, J. Carwardine et al., *The International
477 Linear Collider Technical Design Report - Volume 3.I: Accelerator & in the Technical Design Phase*,
478 [1306.6353](#).
- 479 [4] C. Adolphsen, M. Barone, B. Barish, K. Buesser, P. Burrows, J. Carwardine et al., *The International
480 Linear Collider Technical Design Report - Volume 3.II: Accelerator Baseline Design*, [1306.6328](#).
- 481 [5] H. Abramowicz et al., *The International Linear Collider Technical Design Report - Volume 4:
482 Detectors*, [1306.6329](#).
- 483 [6] J.-C. Bréant and H. Videau, *The Calorimetry at the future e+ e- linear collider*, *eConf* **C010630**
484 (2001) E3047, [[hep-ex/0202004](#)].
- 485 [7] V. Morgunov and A. Raspereza, *Novel 3-D clustering algorithm and two particle separation with tile
486 HCAL*, in *Linear colliders. Proceedings, International Conference, LCWS 2004, Paris, France, April
487 19-23, 2004*, pp. 431–436, 2004. [physics/0412108](#).
- 488 [8] F. Sefkow, A. White, K. Kawagoe, R. Pöschl and J. Repond, *Experimental Tests of Particle Flow
489 Calorimetry*, *Rev. Mod. Phys.* **88** (2016) 015003, [[1507.05893](#)].

- 490 [9] CALICE collaboration, C. Adloff, J. Blaha, J. J. Blaising, C. Drancourt, A. Espargiliere, R. Galione
491 et al., *Tests of a particle flow algorithm with CALICE test beam data*, *JINST* **6** (2011) P07005,
492 [[1105.3417](#)].
- 493 [10] CALICE collaboration, J. Repond et al., *Design and Electronics Commissioning of the Physics
494 Prototype of a Si-W Electromagnetic Calorimeter for the International Linear Collider*, *JINST* **3**
495 (2008) P08001, [[0805.4833](#)].
- 496 [11] CALICE collaboration, C. Adloff et al., *Response of the CALICE Si-W electromagnetic calorimeter
497 physics prototype to electrons*, *Nucl. Instrum. Meth.* **A608** (2009) 372–383, [[0811.2354](#)].
- 498 [12] C. Adloff et al., *Study of the interactions of pions in the CALICE silicon-tungsten calorimeter
499 prototype*, *JINST* **5** (2010) P05007, [[1004.4996](#)].
- 500 [13] CALICE collaboration, C. Adloff et al., *Effects of high-energy particle showers on the embedded
501 front-end electronics of an electromagnetic calorimeter for a future lepton collider*, *Nucl. Instrum.
502 Meth.* **A654** (2011) 97–109, [[1102.3454](#)].
- 503 [14] CALICE collaboration, B. Bilki et al., *Testing hadronic interaction models using a highly granular
504 silicon-tungsten calorimeter*, *Nucl. Instrum. Meth.* **A794** (2015) 240–254, [[1411.7215](#)].
- 505 [15] GEANT4 collaboration, S. Agostinelli et al., *GEANT4: A Simulation toolkit*, *Nucl. Instrum. Meth.*
506 **A506** (2003) 250–303.
- 507 [16] J. Allison et al., *Geant4 developments and applications*, *IEEE Trans. Nucl. Sci.* **53** (2006) 270.
- 508 [17] J. Allison et al., *Recent developments in GEANT4*, *Nucl. Instrum. Meth.* **A835** (2016) 186–225.
- 509 [18] CALICE collaboration, R. Cornat and R. Pöeschl, *Technological prototype of a silicon-tungsten
510 imaging electromagnetic calorimeter*, *JINST* **10** (2015) C06015.
- 511 [19] CALICE collaboration, R. Cornat, *Semiconductor sensors for the CALICE SiW EMC and study of the
512 cross-talk between guard rings and pixels in the CALICE SiW prototype*, *J. Phys. Conf. Ser.* **160**
513 (2009) 012067.
- 514 [20] S. Callier, F. Dulucq, C. de La Taille, G. Martin-Chassard and N. Seguin-Moreau, *SKIROC2, front
515 end chip designed to readout the Electromagnetic CALorimeter at the ILC*, *JINST* **6** (2011) C12040.
- 516 [21] F. Gastaldi, R. Cornat, F. Magniette and V. Boudry, *A scalable gigabit data acquisition system for
517 calorimeters for linear collider*, *PoS TIPP2014* (2014) 193.
- 518 [22] M. Rubio-Roy, F. Thiant and F. Magniette, *Flexible online monitoring for high-energy physics with
519 Pyrame*, *J. Phys. Conf. Ser.* **898** (2017) 032009.
- 520 [23] CALICE collaboration, F. Magniette and A. Irles, *Pyrame 3, an online framework for Calice
521 SiW-Ecal*, *JINST* **13** (2018) C03009.
- 522 [24] M. S. Amjad et al., *Beam test performance of the SKIROC2 ASIC*, *Nucl. Instrum. Meth.* **A778** (2015)
523 78–84.
- 524 [25] V. Boudry, R. Cornat, D. Lacour, R. Pöschl and F. Magniette, *Advanced assembly chain for Si
525 calorimeters*, .
- 526 [26] T. Suehara et al., *Performance study of SKIROC2/A ASIC for ILD Si-W ECAL*, *JINST* **13** (2018)
527 C03015, [[1801.02024](#)].
- 528 [27] CALICE collaboration, A. Irles, *Latest R&D news and beam test performance of the highly granular
529 SiW-ECAL technological prototype for the ILC*, *JINST* **13** (2018) C02038, [[1802.08806](#)].

- 530 [28] CALICE collaboration, A. Irles, *Latest developments on the highly granular Silicon-Tungsten*
531 *Electromagnetic Calorimeter technological prototype for the International Large Detector*, in 2017
532 *IEEE Nuclear Science Symposium and Medical Imaging Conference (NSS/MIC 2017) Atlanta,*
533 *Georgia, USA, October 21-28, 2017*, 2018. [1801.10407](#).